ACS APPLIED NANO MATERIALS

www.acsanm.org Article

$MoTe_2$-Based Schottky Barrier Photodiode Enabled by Contact Engineering

Inayat Uddin, Nhat Anh Nguyen Phan, Hai Yen Le Thi, Hanul Kim, Dongmok Whang, and Gil-Ho Kim*

Cite This: https://doi.org/10.1021/acsanm.2c04569 Read Online

ACCESS | Metrics & More | Article Recommendations | Supporting Information

ABSTRACT: Two-dimensional (2D) atomic crystalline materials have attracted the scientific community owing to their remarkable electrical and optical applications, such as solar cells, light-emitting diodes, and photodiodes. This study demonstrates a Schottky barrier photodiode (SPD) using different metal architectures in lateral and vertical contacts on n-type 2H phase semiconducting molybdenum ditelluride ($MoTe_2$) synthesized by the self-flux crystal growth method. High-work-function palladium and low-work-function indium metals have been deposited on $MoTe_2$ to fabricate a field-effect transistor confirming diode characteristics. The device shows an ideality factor of 1.09 and a rectification ratio of 10^2, indicating ideal diode characteristics based on a single $MoTe_2$ channel. In addition, we measured the device in the dark and used the green laser to analyze the photodiode behavior of SPD in a wide range of light intensity. A single channel using contact architecture-based study is helpful to apply in other 2D materials to achieve the simplest fundamental diodes for future nanoelectrical and optoelectronic devices.

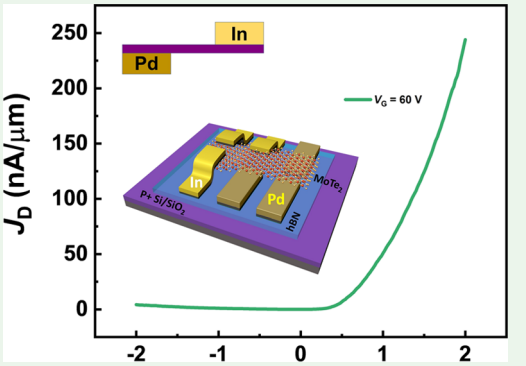

KEYWORDS: *Schottky photodiode, $MoTe_2$, flux method, contact engineering, p-n junction*

1. INTRODUCTION

Transition metal dichalcogenides (TMDs) have become the focus of material class for intense research due to their exceptional physical and chemical features, such as thickness-dependent electronic properties, free dangling bond surface, mechanical flexibility, and excellent intrinsic carrier mobility.[1−4] TMDs, due to their flexibility, are stacked in different configurations to fabricate devices, allowing for modifying the physical properties based on the structure for future applications.[5,6] As a result, they have received a lot of interest in electronic and optoelectronic applications, such as field-effect transistors (FETs), spintronics, solar cells, light-emitting diodes, and photodetectors.[7−11] Specifically, extensive studies have been done, where TMD diodes are stacked in p- and n-type materials for a variety of applications as switching devices, photodetectors, and self-powered sensors, by producing depletion regions to rectify unidirectional current.[12−14] Among them, 2H phase semiconducting molybdenum ditelluride ($MoTe_2$) exhibits a relatively low band gap such as a direct optical band gap of 1.02 eV in a monolayer. In comparison, its multilayered form shows an indirect band gap of 0.85 eV, which benefits it in a broader spectrum response.[15−17] In addition, $MoTe_2$ absorbs light from visible to near-infrared wavelengths, making it an excellent material for photoresponse behavior.[18] The Schottky barrier photodiode (SPD) is a structure that does not stack in a heterostructure and consumes less power than conventional p-n diodes due to its rapid response and minimal voltage drop in the forward direction.[19] Studies have been reported that revealed exceptional diode properties in two-dimensional (2D) p-n junction heterostructures. However, the SPD based on contact engineering is yet to be explored extensively for practical use.[20]

In this work, a single-channel $MoTe_2$-based FET device is fabricated in a lateral and vertical structure using high and low work function metal contact to study the comparative electrical charge transport properties. The designed electrodes consist of direct palladium (Pd) contact with $MoTe_2$ on the bottom and indium (In) on the top of the channel covered by gold (Au) metal layers to avoid degradation due to oxidation. The electrical charge transport properties are investigated in lateral and vertical structures, such as on bottom contacts (Pd−Pd), top contacts (In−In), and from top to bottom contacts (In−Pd) in an intrinsic $MoTe_2$ FET. In the lateral structures, the device shows ohmic and Schottky contacts, whereas the

Received: October 19, 2022
Accepted: December 20, 2022

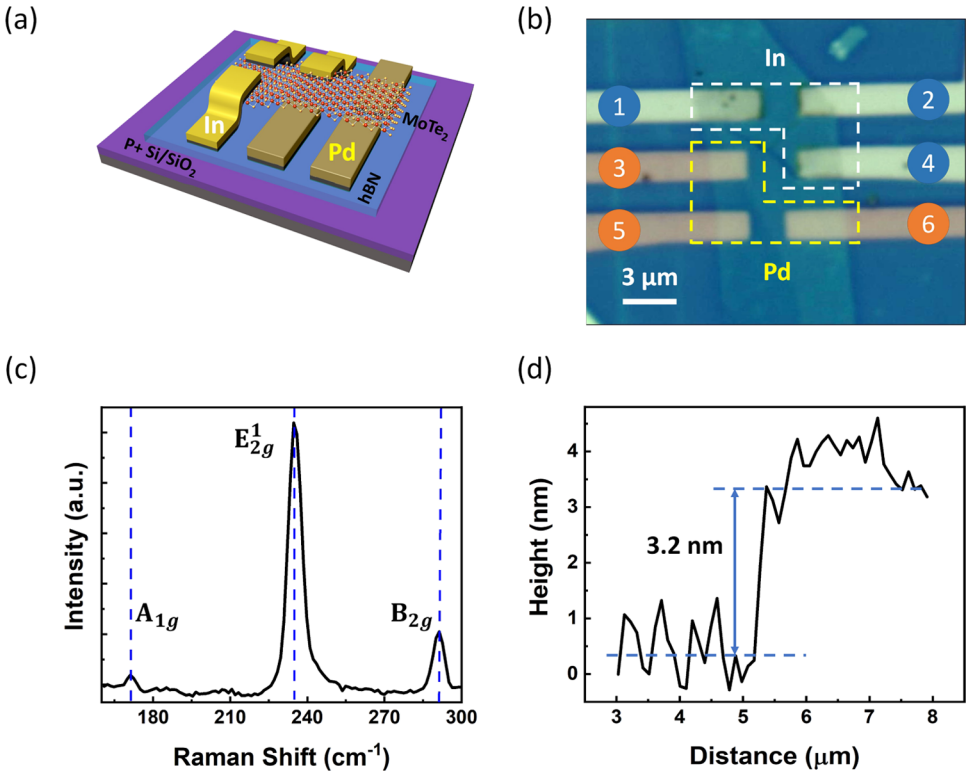

Figure 1. Lateral and vertical metal contact engineering in the $MoTe_2$ FET. (a) Schematic illustration of the $MoTe_2$ SPD device. (b) Optical image of the $MoTe_2$ SPD device with top In and bottom Pd metal contacts. (c) Raman spectra obtained from the $MoTe_2$ flake with atomic displacements showing vibrational modes. (d) AFM line profile shows the thickness of the $MoTe_2$ flake.

vertical structure across top−bottom contacts shows p-n junction characteristics. In fabrication, Pd metal with high work function (Φ = 5.6 eV)[21] due to its good air stability and resistance to oxidation is deposited on the bottom of a mechanically exfoliated multilayer $MoTe_2$, while In metal with low work function (Φ = 4.1 eV)[22] is deposited on the top surface of the flake, which exhibits as an ideal-like diode upon measuring from top to bottom contacts. Uneven metal contacts resulted in an ideality factor of 1.09, and a rectification ratio of up to 10^2 was observed at room temperature. Unlike complex p-n junction diodes, our simplified structure can be applied to compare charge transport properties at various temperatures and photodiode behavior, such as mobility, ideality factor, and tunneling barrier height.

2. RESULTS AND DISCUSSION

Figure 1a illustrates the schematic diagram of $MoTe_2$ SPD, whereas Figure 1b shows the optical image of the device on which Pd high-work-function electrodes are designed to the bottom and In low-work-function electrodes on the top of the multilayered $MoTe_2$. First, thick hexagonal boron nitride (h-BN) was transferred on a precleaned Si/SiO_2 1 × 1 cm^2 wafer to prevent the leakage current and interface traps.[23] Pd owing to its stability in the air was patterned on h-BN and mechanically exfoliated multilayered flakes from our grown $MoTe_2$ bulk crystals transferred onto prepatterned Pd electrodes using a dry transfer method with poly-(dimethylsiloxane) (PDMS) stamp. Later, In electrodes were designed on the top surface of the $MoTe_2$ multilayered channel. To obtain Raman spectra of the n-type $MoTe_2$ flake, we used the excitation laser of 532 nm wavelength in an ambient environment at room temperature.

The Raman spectrum in Figure 1c shows three peaks of $MoTe_2$:A_{1g} mode at a peak value of 170 cm^{-1}, E^1_{2g} mode at a peak value of 234 cm^{-1}, and B^1_{2g} mode at a peak value of 289 cm^{-1}.[24] Atomic force microscopy (AFM) was performed to confirm the layer thickness or the number of layers of the $MoTe_2$ flake, as shown in Figure 1d. The layer thickness of $MoTe_2$ was 3.2 nm, confirming that the $MoTe_2$ flake was approximately four layers,[25] as shown by drawing a white line in Figure S2.

The output characteristics normalized by the channel width of In−In contacts on $MoTe_2$ at various gate biases are shown in Figure 2a, which shows an ohmic-like junction with low resistance based on the linear output characteristics. On the other hand, bottom (Pd−Pd) contacts have nonlinear output characteristics, generating Schottky junctions with high resistive contacts, as shown in Figure 2c. The transfer characteristics normalized by the channel width of the lateral metal−$MoTe_2$−metal with top In−In contact and bottom Pd−Pd contact are shown in Figure 2b,d as a function of the drain voltages. The device demonstrated ambipolar behavior with n-type electron dominant features for both connections at different drain voltages. Due to the difference in Fermi levels, when an n-type semiconductor meets metal with a higher work function, the electrons of the semiconductor diffuse into the metal with a lower energy state, generating a depletion area until aligned Fermi level. Thus, a potential is created, which blocks carrier injection into metal and forms the Schottky junction. On the other hand, when the n-type semiconductor meets low-work-function metal, it starts aligning the Fermi level and the electrons move from semiconductor to metal due to its lower work function than metal, forming ohmic contact.[26,27] The field-effect mobility (μ_{FE}) of the $MoTe_2$

https://doi.org/10.1021/acsanm.2c04569
ACS Appl. Nano Mater. XXXX, XXX, XXX−XXX

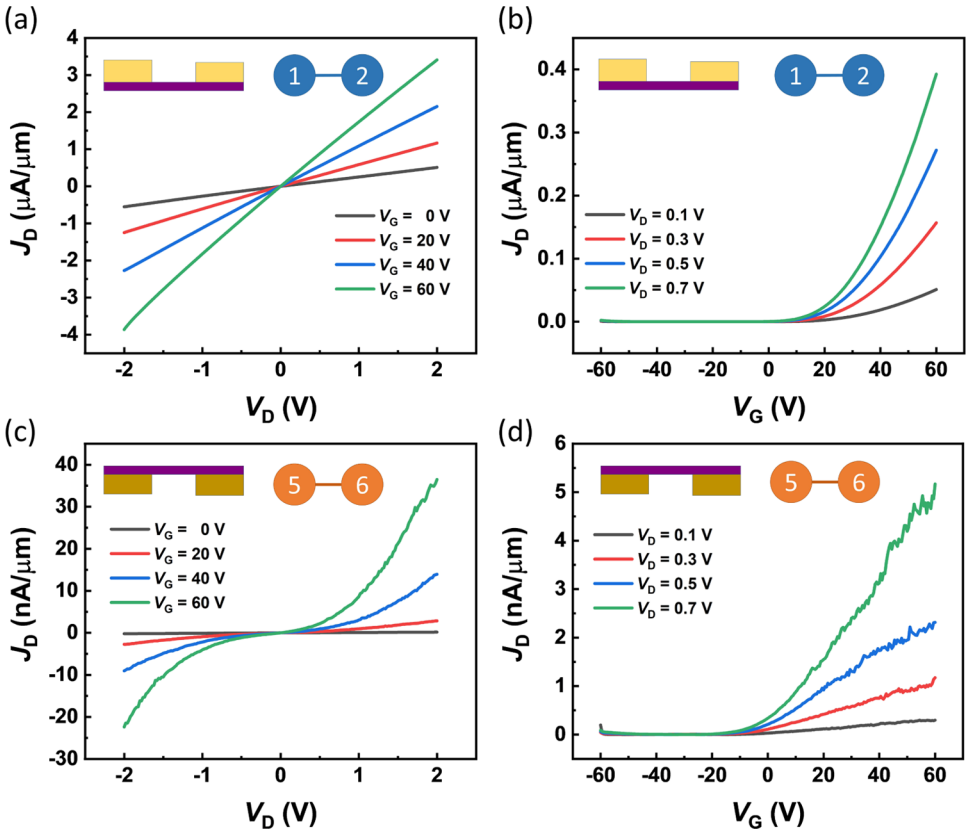

Figure 2. Comparison plot of output and transfer characteristics normalized by the channel width for different electrode architectures at a temperature of 300 K. (a) Output characteristics of In−In contact at the top of the $MoTe_2$ single channel depending on different gate biases. (b) Transfer characteristic plot of the $MoTe_2$ single channel at different drain voltages. (c) Output characteristic plot of Pd−Pd contact at the top of the $MoTe_2$ single channel depending on different gate biases. (d) Transfer characteristic plot of the $MoTe_2$ single channel at different drain voltages.

device with different contact architectures (In−In, Pd−Pd, and In−Pd) is calculated using $\mu_{FE} = g_m \times \left[\frac{L}{WC_{ox}V_{DS}}\right]$, where $g_m = (dI_{DS}/dV_G)$ is the transconductance, L is the channel length, W is the width, C_{ox} is the capacitance of 285 nm thick SiO_2, I_D is the source−drain current, V_D represents the drain voltage, and V_G is the gate voltage.[28] The electron mobility at room temperature in the lateral structure for In−In contact is 60.04 $cm^2\ V^{-1}\ s^{-1}$ with a current on/off ratio of 10^5 at V_D = 0.1 V, while for Pd−Pd connection, the electron mobility is found to be 0.31 $cm^2\ V^{-1}\ s^{-1}$ with a current on/off ratio of 10^2. By contrast, the electron mobility in the vertical structure for In−Pd contacts is obtained at 0.17 $cm^2\ V^{-1}\ s^{-1}$ with a current on/off ratio of 10^3. Thus, our findings suggest that the electrical connection is much improved in the top contact with In−$MoTe_2$ instead of Pd−$MoTe_2$. It can be referred to as the good ohmic contact formation at the metal−semiconductor junction due to the low-work-function value of In and n-type dominant nature of $MoTe_2$. The on/off ratios for lateral and vertical structures are extracted from the logarithmic scale of transfer characteristic curves as shown in Figure S3.

At the metal−semiconductor interface, a charge carrier hinders by a barrier that includes a major carrier transport mechanism explained by thermionic emission theory.[29−32] In Figure 3a, the output characteristics normalized by the channel width (inset: logarithmic scale) of In and Pd electrodes show strong rectification behavior as a function of gate biases ranging from 0 to 60 V. At the Pd semiconductor junction, a high barrier is formed in the reverse direction of the diode. While in contact with low work function, the In semiconductor junction forms an ohmic junction with $MoTe_2$ in the diode's forward direction. Thus, a high resistive barrier at the junction of Pd exists, and the $MoTe_2$ device exhibits an ideal diode behavior. Figure 3b shows the transfer characteristics normalized by the channel width for different metal architectures, showing an n-type $MoTe_2$ behavior and an increase in the current varying drain voltages at room temperature. Figure 3c shows the logarithmic plot of output characteristics at room temperature. The $MoTe_2$ device exhibits rectifying behavior with increased drain current by increasing the gate voltage. The rectifying performance of the Schottky diode in different metal architectures can be estimated by evaluating the ideality factor (η), which can be determined using the Shockley diode equation.[33,34] The ideality factor can be figured out from a plot of the natural logarithm of the diode current vs drain voltage by taking the slope, which gives $e/\eta k_B T$.[19,20] In our device, the lowest ideality factor is found to be 1.09 at room temperature, which is close to unity. The ideal diode-like behavior can be obtained if the ideality factor is closer to unity. The ideality factor increases upon the decrease in current as the forward current is mainly based on the diffusion of electrons. The ideality factor is strongly temperature-dependent, which is calculated at the slope of forward-biased region temperature ranging from 77 to 300 K. Figure 3d shows the variation in ideality factor with a decrease in temperature from 300 to 77 K. Our device has a

https://doi.org/10.1021/acsanm.2c04569
ACS Appl. Nano Mater. XXXX, XXX, XXX−XXX

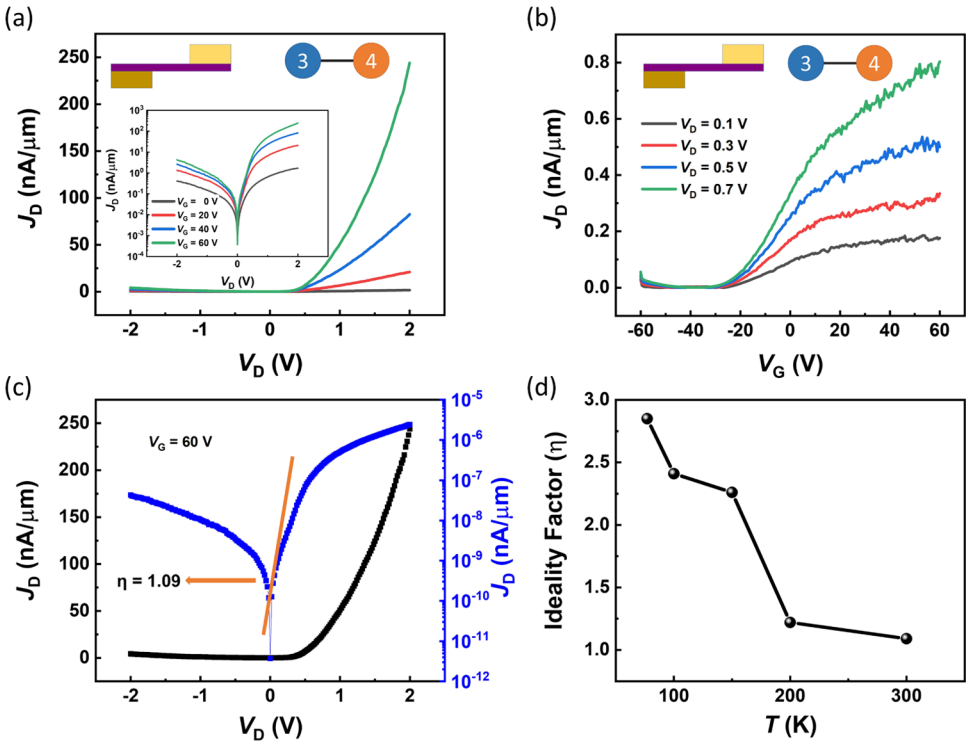

Figure 3. Plot of SPD behavior of the $MoTe_2$-based device at a temperature of 300 K. (a) Output characteristics normalized by the channel width of the $MoTe_2$ device on the top to bottom contact as a function of gate bias. Inset: Logarithmic scale of output characteristics at various gate biases. (b) Transfer characteristics normalized by the channel width of the $MoTe_2$ device on the top to bottom contact at different drain voltages. (c) Plot of the natural logarithm of the diode current vs drain voltage to determine the ideality factor. (d) Ideality factor of the SPD as a function of temperature.

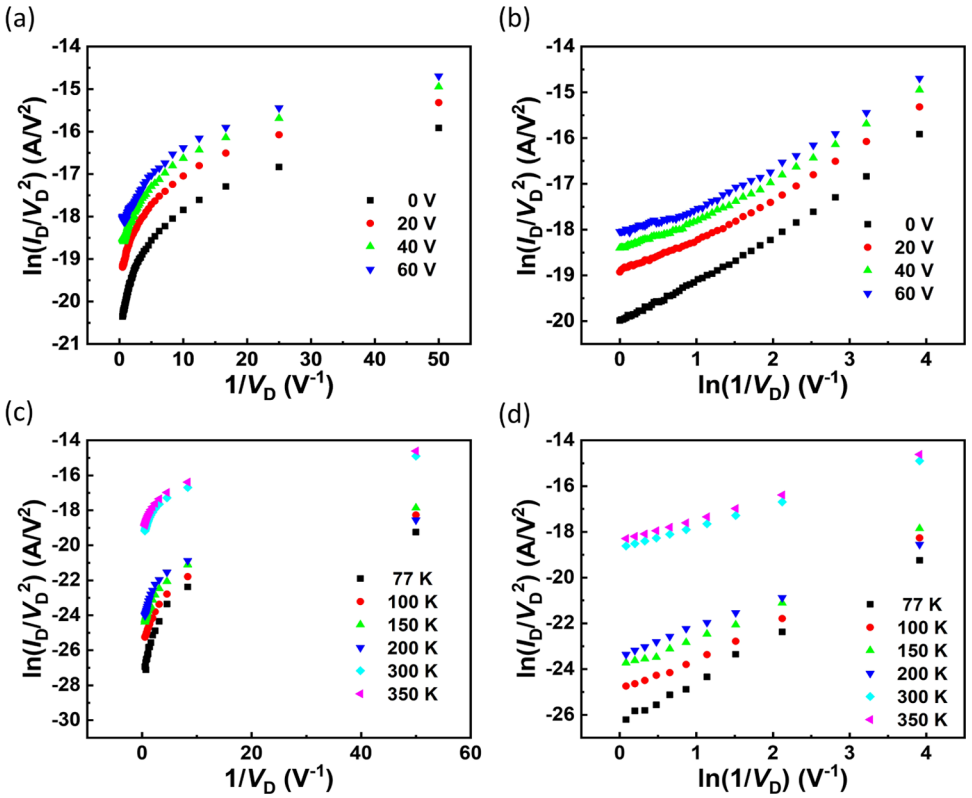

Figure 4. (a) Plot of $\ln(I/V_D^2)$ as a function of $(1/V_D)$ illustration of the DT behavior of the device at various gate biases at room temperature. (b) Plot of $\ln(I/V_D^2)$ vs $\ln(1/V_D)$ at different gate biases. (c) Plot of $\ln(I/V_D^2)$ as a function of $(1/V_D)$ illustration of the DT behavior of the device at V_G = 60 V. (d) Plot of $\ln(I/V_D^2)$ vs $\ln(1/V_D)$ at different temperatures showing linear relation of DT of the device.

https://doi.org/10.1021/acsanm.2c04569
ACS Appl. Nano Mater. XXXX, XXX, XXX−XXX

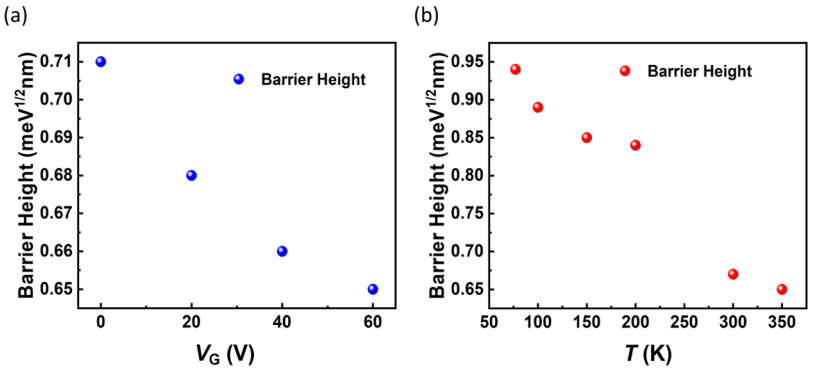

Figure 5. Barrier parameter calculation. (a) Tunneling barrier height of the $MoTe_2$ device as a function of gate bias at a temperature of 300 K. (b) Tunneling barrier height of the $MoTe_2$ device as a function of temperature.

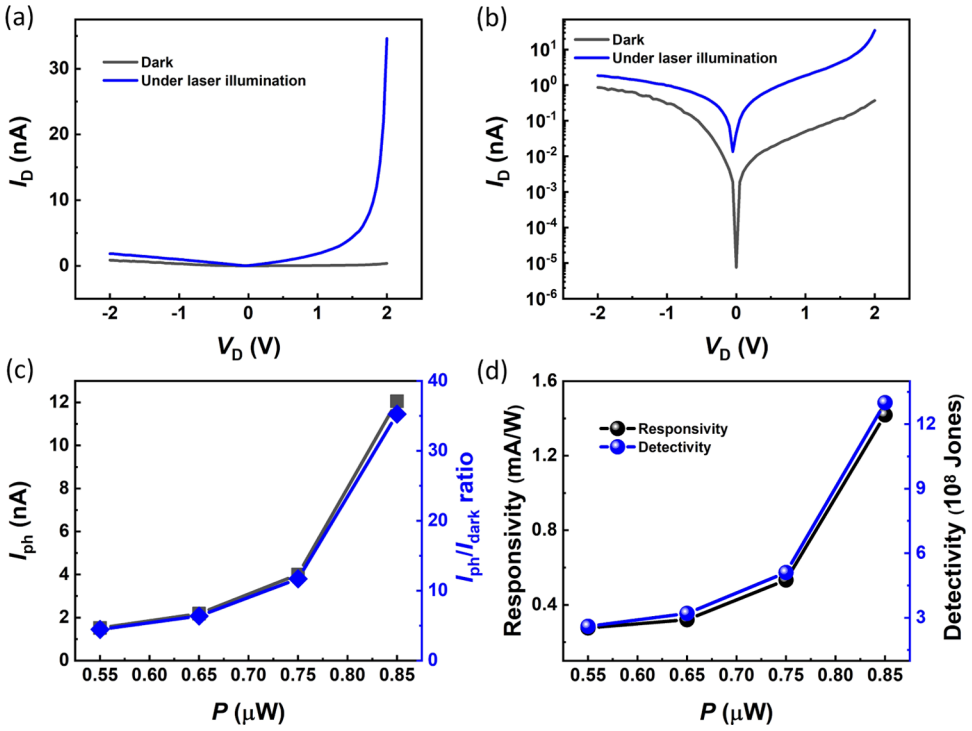

Figure 6. Photoresponse of the $MoTe_2$ SPD at room temperature in an ambient environment (a) Output characteristic plot of the $MoTe_2$ device in the top-to-bottom contact under the λ = 520 nm green laser illumination and dark conditions. (b) Logarithmic scale of output characteristic plots of the $MoTe_2$ device. (c) Plot of the photocurrent (I_{ph}) and (I_{ph}/I_{dark}) ratio as a function of power. (d) Plot of the responsivity and detectivity of the $MoTe_2$ SPD as a function of power.

lower ideality factor of 1.09, which is close to unity at 300 K, while a higher ideality factor of 2.85 at a lower temperature of 77 K, showing strong dependence on temperature, as shown in Figure S4. We refer to the higher ideality factor at low temperatures as the current through the metal−semiconductor junction depends upon temperature and electrons only can overwhelm the lower barrier resulting in deviation in ideality.

To explore the vertical charge transport, we measured our device in a range of temperatures from 77 to 350 K shown in Figures S5 and S6, as both contact resistance and interlayer resistance effectively contribute to the total resistance. Our device shows Schottky contact at the barrier interface, and charge transfer across the barrier is dominant due to the tunneling behavior. At low bias voltages, direct tunneling (DT) is dominated, which can be approximated by the following equation[35−38]

$$I = \frac{Aq^2V\sqrt{2m^*\varnothing_B}}{h^2d}\exp\left(-\frac{4\pi d\sqrt{2m^*\varnothing_B}}{h}\right) \quad (1)$$

At higher bias voltages, the probability of tunneling is increased as the barrier is reshaped from a trapezoid to a triangle, where the Fowler−Nordheim tunneling (FNT) is dominant, which can be described by the following equation[35−38]

$$I = \frac{Aq^3m_0V^2\sqrt{2m^*\varnothing_B}}{8\pi h\varnothing_B d^2m^*}\exp\left(-\frac{8\pi d\sqrt{2m^*}\varnothing_B^{3/2}}{3hqV}\right) \quad (2)$$

In eqs 1 and 2, $\varnothing_B$ is the tunneling barrier height, m_0 is the rest electron mass, m^* (0.46 m_0)[32] is the effective mass of electrons in the $MoTe_2$ flake, q is an electronic charge, h is Planck's constant, A is the electrical contact area, and d is the

https://doi.org/10.1021/acsanm.2c04569
ACS Appl. Nano Mater. XXXX, XXX, XXX−XXX

width of the interface barrier. The plot of $\ln(I/V_D^2)$ vs $(1/V_D)$ curves shown in Figure 4a,c illustrated two different plots at various gate voltages and temperatures ranging from 77 to 350 K. The device exhibits exponential behavior, indicating that DT is the dominant charge carrier mechanism, while FNT is not observed. However, the DT and FNT are observed at a transition voltage of V_T = 1.1 V by measuring the device in an ambient environment under green laser illumination using the wavelength of 520 nm shown in Figure S7. To further confirm the DT mechanism, we plotted $\ln(I/V_D^2)$ as a function of $\ln(1/V_D)$, where the plots illustrated the linear relation as shown in Figure 4b,d. Furthermore, it is used to obtain the DT barrier parameters $d\sqrt{(\varnothing_B)}$ of the SPD device by linear fitting. Figure 5a shows the tunneling barrier height vs the gate voltage of the SPD device. The tunneling barrier height has a decreasing trend and varies in the range of $(0.71-0.65\ \mathrm{meV}^{1/2})$ nm.

Similarly, a decrease in tunneling barrier height in the range of $(0.94-0.65)\ \mathrm{meV}^{1/2}$ nm is observed depending on the temperature range from 77 to 350 K. High tunneling barrier height can be seen at a low temperature (77 K) while low tunneling barrier height is observed at a high temperature (350 K) as shown in Figure 5b. The above results illustrate that tunneling barrier height depends upon gate voltage and temperature. We refer to these variations in barrier parameters as the inhomogeneity and interfacial surface defects that are present at the metal−semiconductor interface.[19]

In addition, we demonstrated the photodiode behavior of the $MoTe_2$ device under green laser light illumination with a wavelength (λ) of 520 nm and a wide range of power intensity in the top to bottom contacts (In−Pd). Under the illumination of green laser light of a wide range of power intensities, the SPD shows good photodiode behavior as shown in Figure 6a,b. The responsivity and detectivity are the key parameters that were evaluated for the $MoTe_2$ SPD device at V_D = 1 V. The responsivity is defined as $R = I_{ph}/P$, in which P is the power of incident illumination, and I_{ph} is the photocurrent, which is calculated by the equation: $I_{ph} = I_{light} - I_{dark}$, where I_{light} and I_{dark} are the current measured under light illumination and dark conditions. The photocurrent is increasing with an increase in incident laser power intensity as shown in Figure 6c. The detectivity is defined by the equation $D = R/\sqrt{2qI_{dark}}$, where both the responsivity and detectivity are estimated as 1.4 mA W^{-1} and 13.5×10^8 Jones, respectively, at P = 0.85 μW under the λ = 520 nm green laser light as shown in Figure 6d. Moreover, the device was measured in an ambient environment due to the limitation of the facility. Thus, the polarity was changed from n-type to p-type, as shown in Figure S8. As earlier published reports have revealed that deep ultraviolet irradiations, electrostatic gating, and chemical doping of the TMDs can change the intrinsic operation of the device.[39−42]

However, in our device, we refer to polarity conversion to the hole doping in the air as the energy level difference that exists between $MoTe_2$ (4.1 eV) and oxygen/water redox couple (4.83 eV) due to which the electrons are injected from $MoTe_2$ to oxygen/water redox couple.[43]

3. CONCLUSIONS

In summary, we have fabricated FETs using different metal architectures in lateral and vertical contacts on n-type $MoTe_2$ grown by the self-flux method to study electrical charge transport properties. Due to the difference in the work function of deposited metal electrodes, the electrical charge transport in the top to bottom contacts at various gate biases confirmed ideal-like diode characteristics giving an ideality factor of 1.09, which is close to the unity. This value demonstrates an ideal-like diode behavior obtained in a simple single channel regardless of the complex diode structure that usually requires a heterostructure based on p- and n-type materials. The device shows excellent electrical properties on the top contacts between (In−In) contacts over a wide range of temperatures. In addition, the device shows a stable photodiode response to the green laser light, confirming the application of a single-channel diode for future electrical and optoelectronic devices.

4. EXPERIMENTAL METHODS

4.1. $MoTe_2$ Crystals Grown by the Self-Flux Method. The self-flux method is used to grow $MoTe_2$ crystals, and tellurium was used as a self-flux material and a reactive agent as shown in Figure S1a. The growth of exceptionally pure crystals is made possible by the flux material having a lower melting point, which aids in dissolving solute for the chemical reaction and crystallization process. Removing the flux material from the grown crystals requires immediate centrifugation. The source materials molybdenum powder of purity 99.99% (Sigma Aldrich) and tellurium 99.999% (Alfa Aesar) were measured and added into an alumina crucible fixed into a quartz tube ampule in Argon (Ar) environment inside a glovebox. A cylindrical shape of high purity 99.99% SiO_2 quartz wool with excellent insulation performance was also loaded above one cm of alumina crucible to absorb excessive solvent in centrifugation. It is then placed into a high-temperature furnace while being vacuum sealed. The furnace temperature program was set at 1100 °C as a ramp-up temperature at 50 °C h^{-1}. The temperature dwelling time was set for 36 h, and then, the ampule was allowed to cool down at 2.5 °C h^{-1} until it reached 550 °C. The resultant ampule was centrifuged at 2000 rpm for 120 s to the obtained large size of about 0.6 cm crystals as shown in Figure S1b. X-ray diffraction was used to characterize the grown crystals to confirm crystal formation and quality as shown in Figure S1c. The formed crystals were then used for device fabrication.

4.2. Device Fabrication. Using the photolithography method, a highly p-doped 285 nm Si/SiO_2 substrate was used to draw an outer electrode pattern, and Au/In metal layers were deposited using an electron beam evaporator before being lifted off in acetone. To prevent leakage current and lessen the scattering, a thick mechanically exfoliated h-BN was transferred using the traditional PDMS stamping method onto a prepatterned substrate. The sample was then cleaned with acetone and isopropyl alcohol, submerged in chloroform and dried using a nitrogen gun. Next, poly(methyl methacrylate) was spin-coated onto the sample and using an e-beam lithography technique, the inner bottom electrodes were drawn on h-BN. After that, Pd/In electrodes were kept at a thickness of 10/5 nm using an electron beam evaporator since Pd exhibits high resistance to oxidation under ambient conditions. Mechanically exfoliated $MoTe_2$ flake was transferred onto metal electrodes by the dry transfer method. Again, metal layers of Au/In 30/10 nm were then deposited onto the $MoTe_2$ flake as top electrodes.

4.3. Device Characterization. X-ray diffraction (XRD) was performed to confirm the $MoTe_2$ crystal growth. After device fabrication, the thickness of $MoTe_2$ was analyzed by AFM in noncontact mode. The Raman analysis of $MoTe_2$ was performed using a laser wavelength of 532 nm under ambient conditions to characterize the flake quality and surface.

4.4. Electrical and Photo Measurements. The electrical transport measurement of the $MoTe_2$ device was performed under a vacuum using a Keithley 4200-SCS parameter analyzer. Photo measurement was performed in the dark and using a 520 nm green laser in the ambient environment using different power intensities.

https://doi.org/10.1021/acsanm.2c04569
ACS Appl. Nano Mater. XXXX, XXX, XXX−XXX

■ ASSOCIATED CONTENT

Supporting Information

The Supporting Information is available free of charge at https://pubs.acs.org/doi/10.1021/acsanm.2c04569.

Crystal growth by the self-flux method; AFM image and line scan profile for $MoTe_2$; electrical characterization of the $MoTe_2$ device at 300 K; ideality factor of $MoTe_2$ SPDs at different temperatures; temperature-dependent electrical characterization; FNT and DT behavior; and optical characteristics (PDF)

■ AUTHOR INFORMATION

Corresponding Author

Gil-Ho Kim − *Department of Electrical and Computer Engineering, Sungkyunkwan University (SKKU), Suwon 16419, Republic of Korea; Sungkyunkwan Advanced Institute of Nanotechnology (SAINT), Sungkyunkwan University (SKKU), Suwon 16419, Republic of Korea;* orcid.org/0000-0002-5153-4235; Email: ghkim@skku.edu

Authors

Inayat Uddin − *Department of Electrical and Computer Engineering, Sungkyunkwan University (SKKU), Suwon 16419, Republic of Korea*

Nhat Anh Nguyen Phan − *Department of Electrical and Computer Engineering, Sungkyunkwan University (SKKU), Suwon 16419, Republic of Korea*

Hai Yen Le Thi − *Sungkyunkwan Advanced Institute of Nanotechnology (SAINT), Sungkyunkwan University (SKKU), Suwon 16419, Republic of Korea*

Hanul Kim − *Sungkyunkwan Advanced Institute of Nanotechnology (SAINT), Sungkyunkwan University (SKKU), Suwon 16419, Republic of Korea*

Dongmok Whang − *Sungkyunkwan Advanced Institute of Nanotechnology (SAINT) and Department of Advanced Materials Science and Engineering, Sungkyunkwan University (SKKU), Suwon 16419, Republic of Korea;* orcid.org/0000-0002-5164-6624

Complete contact information is available at: https://pubs.acs.org/10.1021/acsanm.2c04569

Notes

The authors declare no competing financial interest.

■ ACKNOWLEDGMENTS

This work was supported by the National Research Foundation of Korea (NRF) grant funded by the Korean government (MSIT) (No. 2019R1A2C2088719).

■ ABBREVIATIONS

2D, two-dimensional
SPD, Schottky barrier photodiode
$MoTe_2$, molybdenum ditelluride
TMDs, transition metal dichalcogenides
FETs, field-effect transistors
Pd, palladium
In, indium
Au, gold
h-BN, hexagonal boron nitride
PDMS, poly(dimethylsiloxane)
AFM, atomic force microscopy
μ_{FE}, field-effect mobility
(dI_{DS}/dV_G), transconductance
L, channel length
W, width
C_{ox}, capacitance of 285 nm thick SiO_2
I_D, source−drain current
V_D, drain voltage
V_G, gate voltage
η, ideality factor
DT, direct tunneling
FNT, Fowler−Nordheim tunneling
$\varnothing_B$, tunneling barrier height
m_0, rest electron mass
m^*, effective mass of electrons
q, electronic charge
h, Planck's constant
d, width of the interface barrier.
λ, wavelength

■ REFERENCES

(1) Geim, A. K.; Grigorieva, I. V. Van Der Waals Heterostructures. *Nature* **2013**, *499*, 419−425.

(2) Wang, Q. H.; Kalantar-Zadeh, K.; Kis, A.; Coleman, J. N.; Strano, M. S. Electronics and Optoelectronics of Two-Dimensional Transition Metal Dichalcogenides. *Nat. Nanotechnol.* **2012**, *7*, 699−712.

(3) Lee, I.; Rathi, S.; Lim, D.; Li, L.; Park, J.; Lee, Y.; Yi, K. S.; Dhakal, K. P.; Kim, J.; Lee, C.; Lee, G. H.; Kim, Y. D.; Hone, J.; Yun, S. J.; Youn, D. H.; Kim, G. H. Gate-Tunable Hole and Electron Carrier Transport in Atomically Thin Dual-Channel WSe_2/MoS_2Heterostructure for Ambipolar Field-Effect Transistors. *Adv. Mater.* **2016**, *28*, 9519−9525.

(4) Nguyen, D. A.; Oh, H. M.; Duong, N. T.; Bang, S.; Yoon, S. J.; Jeong, M. S. Highly Enhanced Photoresponsivity of a Monolayer WSe_2 Photodetector with Nitrogen-Doped Graphene Quantum Dots. *ACS Appl. Mater. Interfaces* **2018**, *10*, 10322−10329.

(5) Kang, J.; Zhang, L.; Wei, S. H. A Unified Understanding of the Thickness-Dependent Bandgap Transition in Hexagonal Two-Dimensional Semiconductors. *J. Phys. Chem. Lett.* **2016**, *7*, 597−602.

(6) Fogler, M. M.; Butov, L. V.; Novoselov, K. S. High-Temperature Superfluidity with Indirect Excitons in van Der Waals Heterostructures. *Nat. Commun.* **2014**, *5*, No. 4555.

(7) Lin, Y. F.; Xu, Y.; Lin, C. Y.; Suen, Y. W.; Yamamoto, M.; Nakaharai, S.; Ueno, K.; Tsukagoshi, K. Origin of Noise in Layered $MoTe_2$ Transistors and Its Possible Use for Environmental Sensors. *Adv. Mater.* **2015**, *27*, 6612−6619.

(8) Lin, X.; Yang, W.; Wang, K. L.; Zhao, W. Two-Dimensional Spintronics for Low-Power Electronics. *Nat. Electron.* **2019**, *2*, 274−283.

(9) Hussain, S.; Patil, S. A.; Vikraman, D.; Mengal, N.; Liu, H.; Song, W.; An, K. S.; Jeong, S. H.; Kim, H. S.; Jung, J. Large Area Growth of $MoTe_2$ Films as High Performance Counter Electrodes for Dye-Sensitized Solar Cells. *Sci. Rep.* **2018**, *8*, No. 29.

(10) Bie, Y. Q.; Grosso, G.; Heuck, M.; Furchi, M. M.; Cao, Y.; Zheng, J.; Bunandar, D.; Navarro-Moratalla, E.; Zhou, L.; Efetov, D. K.; Taniguchi, T.; Watanabe, K.; Kong, J.; Englund, D.; Jarillo-Herrero, P. A $MoTe_2$-Based Light-Emitting Diode and Photodetector for Silicon Photonic Integrated Circuits. *Nat. Nanotechnol.* **2017**, *12*, 1124−1129.

(11) Afzal, A. M.; Iqbal, M. Z.; Dastgeer, G.; ul Ahmad, A.; Park, B. Highly Sensitive, Ultrafast, and Broadband Photo-Detecting Field-Effect Transistor with Transition-Metal Dichalcogenide van Der Waals Heterostructures of $MoTe_2$ and $PdSe_2$. *Adv. Sci.* **2021**, *8*, No. 2003713.

(12) Pezeshki, A.; Shokouh, S. H. H.; Nazari, T.; Oh, K.; Im, S. Electric and Photovoltaic Behavior of a Few-Layer α-$MoTe_2$/MoS_2 Dichalcogenide Heterojunction. *Adv. Mater.* **2016**, *28*, 3216−3222.

(13) Zhang, K.; Zhang, T.; Cheng, G.; Li, T.; Wang, S.; Wei, W.; Zhou, X.; Yu, W.; Sun, Y.; Wang, P.; Zhang, D.; Zeng, C.; Wang, X.; Hu, W.; Fan, H. J.; Shen, G.; Chen, X.; Duan, X.; Chang, K.; Dai, N. Interlayer Transition and Infrared Photodetection in Atomically Thin Type-II $MoTe_2/MoS_2$ van Der Waals Heterostructures. *ACS Nano* **2016**, *10*, 3852−3858.
(14) Kim, Y.; Lee, S.; Song, J. G.; Ko, K. Y.; Woo, W. J.; Lee, S. W.; Park, M.; Lee, H.; Lee, Z.; Choi, H.; Kim, W. H.; Park, J.; Kim, H. 2D Transition Metal Dichalcogenide Heterostructures for P- and n-Type Photovoltaic Self-Powered Gas Sensor. *Adv. Funct. Mater.* **2020**, *30*, No. 2003360.
(15) Wei, X.; Yan, F.; Lv, Q.; Zhu, W.; Hu, C.; Patanè, A.; Wang, K. Enhanced Photoresponse in $MoTe_2$ Photodetectors with Asymmetric Graphene Contacts. *Adv. Opt. Mater.* **2019**, *7*, No. 1900190.
(16) Lezama, I. G.; Arora, A.; Ubaldini, A.; Barreteau, C.; Giannini, E.; Potemski, M.; Morpurgo, A. F. Indirect-to-Direct Band Gap Crossover in Few-Layer $MoTe_2$. *Nano Lett.* **2015**, *15*, 2336−2342.
(17) Zhu, M.; Luo, W.; Wu, N.; Zhang, X. A.; Qin, S. Engineering Few-Layer $MoTe_2$ Devices by Co/HBN Tunnel Contacts. *Appl. Phys. Lett.* **2018**, *112*, No. 183102.
(18) Lu, M. Y.; Chang, Y. T.; Chen, H. J. Efficient Self-Driven Photodetectors Featuring a Mixed-Dimensional van Der Waals Heterojunction Formed from a CdS Nanowire and a MoTe2 Flake. *Small* **2018**, *14*, No. 1802302.
(19) Kim, J.; Venkatesan, A.; Phan, N. A. N.; Kim, Y.; Kim, H.; Whang, D.; Kim, G. H. Schottky Diode with Asymmetric Metal Contacts on WS_2. *Adv. Electron. Mater.* **2022**, *8*, No. 2100941.
(20) Aftab, S.; Iqbal, M. W.; Afzal, A. M.; Khan, M. F.; Hussain, G.; Waheed, H. S.; Kamran, M. A. Formation of an $MoTe_2$ Based Schottky Junction Employing Ultra-Low and High Resistive Metal Contacts. *RSC Adv.* **2019**, *9*, 10017−10023.
(21) Duong, N. T.; Lee, J.; Bang, S.; Park, C.; Lim, S. C.; Jeong, M. S. Modulating the Functions of $MoS_2/MoTe_2$ van Der Waals Heterostructure via Thickness Variation. *ACS Nano* **2019**, *13*, 4478−4485.
(22) Kim, B. K.; Kim, T. H.; Choi, D. H.; Kim, H.; Watanabe, K.; Taniguchi, T.; Rho, H.; Kim, J. J.; Kim, Y. H.; Bae, M. H. Origins of Genuine Ohmic van Der Waals Contact between Indium and MoS_2. *npj 2D Mater. Appl.* **2021**, *5*, No. 9.
(23) Lee, C.; Rathi, S.; Khan, M. A.; Lim, D.; Kim, Y.; Yun, S. J.; Youn, D. H.; Watanabe, K.; Taniguchi, T.; Kim, G. H. Comparison of Trapped Charges and Hysteresis Behavior in HBN Encapsulated Single MoS_2 Flake Based Field Effect Transistors on SiO2 and HBN Substrates. *Nanotechnology* **2018**, *29*, No. 335202.
(24) Ruppert, C.; Aslan, O. B.; Heinz, T. F. Optical Properties and Band Gap of Single- and Few-Layer $MoTe_2$ Crystals. *Nano Lett.* **2014**, *14*, 6231−6236.
(25) Luo, H.; Wang, B.; Wang, E.; Wang, X.; Sun, Y.; Liu, K. High-Responsivity Photovoltaic Photodetectors Based on $MoTe_2/MoSe_2$ van Der Waals Heterojunctions. *Crystals* **2019**, *9*, No. 315.
(26) Yang, M. H.; Teo, K. B. K.; Milne, W. I.; Hasko, D. G. Carbon Nanotube Schottky Diode and Directionally Dependent Field-Effect Transistor Using Asymmetrical Contacts. *Appl. Phys. Lett.* **2005**, *87*, No. 253116.
(27) Hughes, M. A.; Homewood, K. P.; Curry, R. J.; Ohno, Y.; Mizutani, T. An Ultra-Low Leakage Current Single Carbon Nanotube Diode with Split-Gate and Asymmetric Contact Geometry. *Appl. Phys. Lett.* **2013**, *103*, No. 133508.
(28) Pradhan, N. R.; Rhodes, D.; Feng, S.; Xin, Y.; Memaran, S.; Moon, B.; Terrones, H.; Terrones, M.; Balicas, L. Field-Effect Transistors Based On. *ACS Nano* **2014**, *8*, 5911−5920.
(29) Chen, J. R.; Odenthal, P. M.; Swartz, A. G.; Floyd, G. C.; Wen, H.; Luo, K. Y.; Kawakami, R. K. Control of Schottky Barriers in Single Layer MoS_2 Transistors with Ferromagnetic Contacts. *Nano Lett.* **2013**, *13*, 3106−3110.
(30) Wang, W.; Liu, Y.; Tang, L.; Jin, Y.; Zhao, T.; Xiu, F. Controllable Schottky Barriers between MoS_2 and Permalloy. *Sci. Rep.* **2014**, *4*, No. 6928.
(31) Wang, J.; Yao, Q.; Huang, C. W.; Zou, X.; Liao, L.; Chen, S.; Fan, Z.; Zhang, K.; Wu, W.; Xiao, X.; Jiang, C.; Wu, W. W. High Mobility MoS_2 Transistor with Low Schottky Barrier Contact by Using Atomic Thick H-BN as a Tunneling Layer. *Adv. Mater.* **2016**, *28*, 8302−8308.
(32) Kim, J.; Venkatesan, A.; Kim, H.; Kim, Y.; Whang, D.; Kim, G. H. Improved Contact Resistance by a Single Atomic Layer Tunneling Effect in $WS_2/MoTe_2$ Heterostructures. *Adv. Sci.* **2021**, *8*, No. 2100102.
(33) Turitsyna, E. G.; Webb, S. Simple Design of FBG-Based VSB Filters for Ultra-Dense WDM Transmission ELECTRONICS LETTERS 20th January 2005. *Electron. Lett.* **2005**, *41*, 40−41.
(34) Aftab, S.; Khan, M. F.; Gautam, P.; Noh, H.; Eom, J. $MoTe_2$ van Der Waals Homojunction P-n Diode with Low Resistance Metal Contacts. *Nanoscale* **2019**, *11*, 9518−9525.
(35) Das, S.; Prakash, A.; Salazar, R.; Appenzeller, J. Toward Low-Power Electronics: Tunneling Phenomena in Transition Metal Dichalcogenides. *ACS Nano* **2014**, *8*, 1681−1689.
(36) Ahmed, F.; Choi, M. S.; Liu, X.; Yoo, W. J. Carrier Transport at the Metal-MoS_2 Interface. *Nanoscale* **2015**, *7*, 9222−9228.
(37) Retamal, J. R. D.; Periyanagounder, D.; Ke, J. J.; Tsai, M. L.; He, J. H. Charge Carrier Injection and Transport Engineering in Two-Dimensional Transition Metal Dichalcogenides. *Chem. Sci.* **2018**, *9*, 7727−7745.
(38) Phan, N. A. N.; Noh, H.; Kim, J.; Kim, Y.; Kim, H.; Whang, D.; Aoki, N.; Watanabe, K.; Taniguchi, T.; Kim, G. H. Enhanced Performance of WS_2 Field-Effect Transistor through Mono and Bilayer h-BN Tunneling Contacts. *Small* **2022**, *18*, No. 2105753.
(39) Wu, E.; Xie, Y.; Zhang, J.; Zhang, H.; Hu, X.; Liu, J.; Zhou, C.; Zhang, D. Dynamically Controllable Polarity Modulation of $MoTe_2$ Field-Effect Transistors through Ultraviolet Light and Electrostatic Activation. *Sci. Adv.* **2019**, *5*, No. aav3430.
(40) Aftab, S.; Samiya, M.; Raza, A.; Iqbal, M. W.; Ul Haque, H. M.; Ramachandraiah, K.; Yousuf, S.; Jun, S. C.; Rehman, A. U.; Iqbal, M. Z. A Reversible and Stable Doping Technique to Invert the Carrier Polarity of $MoTe_2$. *Nanotechnology* **2021**, *32*, No. 285701.
(41) Rani, A.; Dicamillo, K.; Khan, A. H.; Paranjape, M.; Zaghloul, M. E. Tuning the Polarity of $MoTe_2$ FETs by Varying the Channel Thickness for Gas-Sensing Applications. *Sensors* **2019**, *19*, No. 2551.
(42) Seo, S. G.; Jeong, J.; Kim, S. Y.; Kumar, A.; Jin, S. H. Reversible and Controllable Threshold Voltage Modulation for N-Channel MoS_2 and p-Channel $MoTe_2$ Field-Effect Transistors via Multiple Counter Doping with ODTS/Poly-L-Lysine Charge Enhancers. *Nano Res.* **2021**, *14*, 3214−3227.
(43) Liu, J.; Wang, Y.; Xiao, X.; Zhang, K.; Guo, N.; Jia, Y.; Zhou, S.; Wu, Y.; Li, Q.; Xiao, L. Conversion of Multi-Layered $MoTe_2$ Transistor Between P-Type and N-Type and Their Use in Inverter. *Nanoscale Res. Lett.* **2018**, *13*, No. 291.

https://doi.org/10.1021/acsanm.2c04569
ACS Appl. Nano Mater. XXXX, XXX, XXX−XXX